Improving quantum yield of upconverting nanoparticles in aqueous media via emission sensitization

Michael D. Wisser,[*,†] Stefan Fischer,[‡,†] Chris Siefe,[†] A. Paul Alivisatos,[‡,¶,§,‖] Alberto Salleo,[*,†] and Jennifer A. Dionne[*,†]

†*Department of Materials Science and Engineering, Stanford University, Stanford, CA 94305, USA*

‡*Materials Sciences Division, Lawrence Berkeley National Laboratory, Berkeley, CA 94720, USA*

¶*Department of Chemistry, University of California, Berkeley, Berkeley, CA 94720, USA*

§*Department of Materials Science and Engineering, University of California, Berkeley, Berkeley, CA 94720, USA*

‖*Kavli Energy NanoScience Institute, Berkeley, CA 94720, USA*

E-mail: mwisser@alumni.stanford.edu; asalleo@stanford.edu; jdionne@stanford.edu

Phone: 510-456-7124; 650-725-1025; 650-736-2286

Abstract

We demonstrate a facile method to improve upconversion quantum yields in Yb,Er-based nanoparticles via emission dye-sensitization. Using the commercially available dye ATTO 542, chosen for its high radiative rate and significant spectral overlap with the green

emission of Er^{3+}, we decorate the surfaces of sub-25-nm hexagonal-phase $Na(Y/Gd/Lu)_{0.8}F_4:Yb_{0.18}Er_{0.02}$ upconverting nanoparticles with varying dye concentrations. Upconversion photoluminescence and absorption spectroscopy provide experimental confirmation of energy transfer to and emission from the dye molecules. Upconversion quantum yield is observed to increase with dye sensitization, with the highest enhancement measured for the smallest particles investigated (10.9 nm in diameter); specifically, these dye-decorated particles are more than 2x brighter than are unmodified, organic-soluble nanoparticles and more than 10x brighter than are water-soluble nanoparticles. We also observe 3x lifetime reductions with dye adsorption, confirming the quantum yield enhancement to result from the high radiative rate of the dye. The approach detailed in this work is widely implementable, renders the nanoparticles water-soluble, and most significantly improves sub-15-nm nanoparticles, making our method especially attractive for biological imaging applications.

Keywords

upconversion, radiative rate, dye sensitization, quantum yield, fluorescence lifetimes, nanoparticles

Photon upconversion (UC) is the process by which the energies of two or more long-wavelength photons are combined to yield a single, shorter-wavelength photon. The ability to convert light from longer to shorter wavelengths is desirable for a variety of applications, including solar energy generation,[1–12] photocatalysis,[13–15] security,[16–18] biological imaging,[19–28] and photodynamic therapy.[29–31] For facile incorporation and improved spatial imaging resolution, upconverting nanomaterials are often preferred over bulk materials, particularly for photovoltaic, bioimaging, and security applications. Despite the long-recognized potential of lanthanide-based upconverting materials, current upconverters are still limited by poor UC efficiencies; to date, the highest NIR-to-visible UC efficiencies demonstrated in nanoparticles are

approximately 5% for irradiances below 100 W/cm^2.[32,33] While several factors contribute to the poor performance of existing materials, perhaps the most influential and difficult to overcome are the low dipole moments endemic to lanthanide ions.[29,34–41] In short, the UC process in lanthanide-based materials relies on the occurrence of radiative transitions (both absorptive and emissive) which are classically forbidden via the parity selection rule.[42] As a result, these transitions exhibit very long radiative lifetimes on the order of hundreds of microseconds. Thus, much of the input energy is lost via faster, nonradiative decay pathways, particularly phonon coupling and surface quenching.[32]

Previous work has overcome this issue by leveraging crystal field effects to reduce the applicability of the parity selection rule. By distorting the host lattice either mechanically[38] or synthetically,[41] we demonstrated 2x performance enhancements in $NaYF_4$:Yb,Er upconverting nanoparticles. Here, we complement these approaches by using a fluorescent dye to sensitize UC emission. Compared to local lattice distortion, this approach selectively influences the radiative rate of only the final emitting state. We achieve significant UC quantum yield enhancements by decorating the surfaces of the upconverting nanoparticles (UCNPs) with ATTO 542, a commercially available dye purchased from ATTO-TEC GmbH (see the supporting information for details regarding the structure of the dye). The gap between the lowest unoccupied molecular orbital (LUMO) and the highest occupied molecular orbital (HOMO) of ATTO 542 is very similar in energy to that separating the $^2H_{11/2}$ and $^4S_{3/2}$ excited states from the $^4I_{15/2}$ ground state in Er^{3+}, enabling efficient energy transfer from Er^{3+} to the dye. The dye is able to radiate light much more efficiently than can Er^{3+} by itself. We compare the performances of UCNPs with and without dye and find that dye sensitization significantly alters the UC emission spectrum and improves UC quantum yield. Excited-state lifetime measurements confirm that the increased radiative rate afforded by the dye is responsible for the observed quantum yield enhancements. We vary both particle diameter as well as dye surface density and find that the

observed enhancements are strongly influenced by particle size but depend only weakly on dye concentration. Regardless of particle size and dye coverage, however, the addition of the dye is found to invariably improve performance. Our results demonstrate the importance and the feasibility of increasing radiative rates in lanthanide-based UC materials and open up a novel and general method of significantly enhancing UCNP quantum yield.

UCNPs were colloidally synthesized using a procedure adapted from Wang et al.[43] For each sample, the particles comprised 18 at. % Yb^{3+} and 2 at. % Er^{3+} doped into a host matrix composed predominantly of β-$NaYF_4$; small amounts of Gd or Lu were substituted for Y as necessary to yield smaller or larger particles, respectively, as desired (see the supporting information for more details). Figure 1a depicts the relevant section of the Er^{3+} energy diagram. In a typical Yb,Er-based upconverting material, emission occurs mainly from the $^2H_{11/2}$, $^4S_{3/2}$, and $^4F_{9/2}$ manifolds as shown. The radiative lifetimes of these transitions are very long (e.g., hundreds of microseconds in β-$NaYF_4$:Yb,Er UCNPs[38]), resulting in the majority of the input energy being wasted via faster, nonradiative pathways. We hypothesized that we could reduce the prevalence of nonradiative decay by introducing a fluorescent dye capable of receiving energy transfer from Er^{3+} before emitting light rapidly and with high yield. The fluorescent dye we use in this work, ATTO 542, peaks in absorption at 542 nm, leading us to predict that the LUMO of the dye should readily accept energy transfer from the $^2H_{11/2}$ and $^4S_{3/2}$ states of Er^{3+}. Furthermore, the manufacturer reports a fluorescence yield for the dye of 93%, and at 3.7 ns its lifetime is roughly 5 orders of magnitude shorter than those of Er^{3+}. We accordingly predict that any losses which might be incurred due to the addition of another energy transfer step will be dwarfed by the enhancements engendered by the dramatic increase in radiation rate and efficiency offered by the dye. Finally, it is worth noting that the dye does not absorb in the NIR, making it unlikely that dye decoration will hinder UCNP excitation. Further details including the absorption spectrum of the dye can be found in the supporting information (SI).

To achieve dye adsorption, the ligands (oleic acid) were stripped from the particles via sonication in a dilute solution of hydrochloric acid in ethanol and water, rendering the nanoparticles hydrophilic. The ligand-stripped particles were then mixed in solution with the dye to induce adsorption (see SI for more details). Adsorption is confirmed using Fourier transform infrared spectroscopy (FTIR). Figure 1b includes FTIR patterns for oleic acid, the as-synthesized (i.e., unmodified) nanoparticles, the dye, and the dye-coated nanoparticles. As shown, the FTIR spectra for oleic acid and the as-synthesized UCNPs are nearly identical, which is to be expected given that oleic acid coats the surfaces of these particles. Conversely, the absorption features near 2900 cm^{-1} characteristic of oleic acid (which correspond to CH_2 and CH_3 stretching modes[44]) are absent in the spectrum for the dye. Instead, the dominant features in the dye spectrum occur near 1700 and 1000 cm^{-1}, likely arising from S=O or C=O and S-O or C-O stretching modes, respectively. Finally, the FTIR pattern corresponding to the dye-coated particles is very similar to that of the dye by itself; this consistency, in conjunction with the observation that the dye molecules precipitate exclusively when centrifuged in a solution also containing the ligand-stripped particles, confirm that the dye is successfully adsorbed onto the surfaces of the nanoparticles.

Emission spectra as well as sample images are shown in Figures 1c-f. In the case of the as-synthesized particles, the emission spectrum under NIR illumination shows the two green peaks and one red peak characteristic of Er^{3+}. In stark contrast, however, the Er^{3+} green peaks are absent from the dye-coated UCNP spectrum, which is dominated instead by a broad peak centered near 580 nm. This peak perfectly matches that of the dye's emission spectrum, evincing successful energy transfer from Er^{3+} ions to the dye molecules. As shown, the addition of the dye also yields a decrease in emission intensity from the Er^{3+} $^4F_{9/2}$ state (i.e., the red peak). Given that the Er^{3+} $^2H_{11/2}$ and $^4S_{3/2}$ manifolds are involved in the sequence which leads to population of the $^4F_{9/2}$ state,[45,46] it is unsurprising that the dye (which draws energy from the

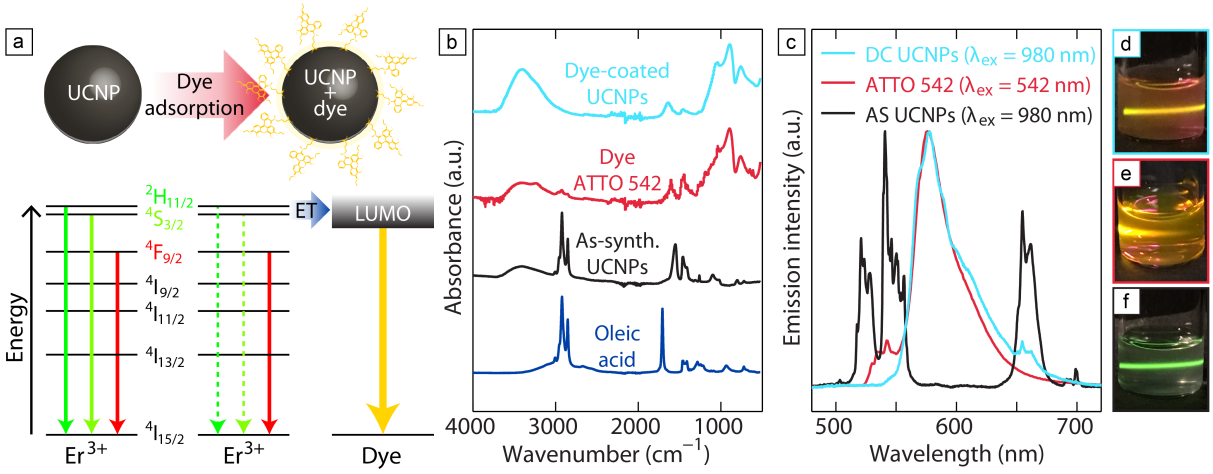

Figure 1: **Concept and demonstration of dye sensitization** a) Schematic summarizing the operating concept in this work. Upconverting nanoparticles ("UCNPs") are decorated with the fluorescent dye ATTO 542, indicated by the orange molecules. The LUMO of this dye is aligned with the $^2H_{11/2}$ and $^4S_{3/2}$ states in Er^{3+}, enabling efficient energy transfer to the dye molecules. b) FTIR patterns providing evidence of dye adsorption. Characteristic CH_2 and CH_3 stretching modes are apparent in the oleic acid (navy) and as-synthesized particle spectra (black) but absent for those of the dye (red) and the dye-coated particles (cyan); these instead show S-O/C-O and S=O/C=O stretching signatures consistent with the structure of the dye. c) Emission spectra of the as-synthesized particles illuminated at 980 nm (black), the bare dye excited directly at 542 nm (red), and the dye-coated particles irradiated at 980 nm (cyan). The emission spectra of the bare dye and the dye-coated UCNPs are almost identical, evincing emission from (and therefore successful energy transfer to) the dye molecules on the UCNPs. The small features present in the dye emission spectrum (red) at 542 nm are experimental artifacts arising from imperfect filtration of the 542-nm excitation source. d-f) Photographs of (d) the dye-coated UCNPs under 980-nm light, (e) ATTO 542 excited at 542 nm, and (f) the as-synthesized particles illuminated at 980 nm. Consistent with the emission spectra, these images highlight the drastic shift induced via dye sensitization.

$^2H_{11/2}$ and $^4S_{3/2}$ states) reduces the likelihood of this population.

We synthesized a series of nanoparticles ranging in diameter from 10.9 $\pm$ 0.8 nm to 25.1 $\pm$ 1.6 nm, as shown in Figure 2, to investigate the impact of dye sensitization as a function of UCNP size. The desired size control was accomplished by adjusting reaction parameters and by carefully tuning the composition of the host matrix from pure $NaYF_4$. Notably, Gd^{3+} was substituted for a fraction of Y^{3+} to produce nanoparticles below 18.5 nm in diameter, and

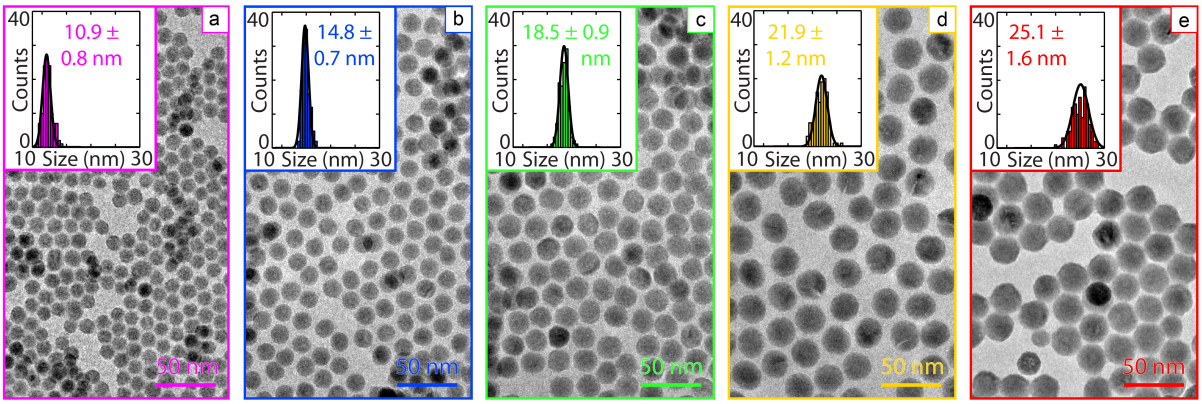

Figure 2: **TEM characterization of β-phase UCNPs** a-e) TEM micrographs showcasing a representative distribution of nanoparticles for each sample used in this work. Particle size histograms, generated by manual measurement of 120 individual particles, are included as insets. Each histogram is fit to a Gaussian, the center of which is taken to be the definitive particle diameter. All samples exhibit standard deviations at or below 7% of the corresponding ensemble size, indicating very low degrees of polydispersity.

a small amount of Lu^{3+} was incorporated to yield particles above 22 nm (see SI for more details). Although our previous work has demonstrated the influence of such modification on UC quantum yield,[41] any similar effects present here will be normalized out as each dye-coated sample is compared to an unmodified sample from the same synthesis. Demonstrated in Figure 2, the samples used in this work exhibit a very high degree of monodispersity, with the standard deviation for each being only 5-7% of the center value. X-ray diffractometry (XRD) is also used to confirm that all of the samples are pure β phase; these data are included in the SI.

Figure 3 summarizes the effect of dye sensitization as a function of UCNP size. For each sample, a constant dye surface density target of 1 molecule per 28 nm^2 of UCNP surface, chosen based on the findings of Zou et al. and others regarding absorption sensitization,[47–49] was maintained (see the SI for further details). We assume that all of the dye added in the adsorption process successfully decorates the UCNPs regardless of particle size. While we do not verify this assumption experimentally, we note that centrifugation of solutions containing both the dye and the ligand-stripped UCNPs yields a brightly colored pellet and a completely clear super-

natant for all particle sizes studied, suggesting that our assumption is valid. Consequently, we use the dye:UCNP mass ratio as a proxy for dye surface density. UC quantum yield, here defined as the number of visible photons emitted divided by the number of NIR photons absorbed, is plotted in Figure 3a as a function of size for the three sample sets used in this study: dye-coated, as-synthesized, and ligand-stripped. As mentioned previously, removing the oleic acid ligands renders the particles hydrophilic and thus insoluble in nonpolar solvents. Therefore, for these measurements the ligand-stripped particles were dispersed in isopropyl alcohol (IPA), while the as-synthesized particles were dispersed in cyclohexane. All UC quantum yield values were obtained under 50 W/cm^2 of 980-nm illumination (values at other irradiances are included the SI). The observed quantum yield difference between these sets of particles arises from the greater prevalence of surface quenching in IPA compared to cyclohexane, which in turn follows from differences in the vibrational mode energies of the two solvents;[50,51] see the SI for further discussion. Additionally, for each sample set, UC quantum yield scales with size due to the reduced prevalence of surface quenching,[11,21,50,52,53] and at every size, the as-synthesized UCNPs outperform the ligand-stripped UCNPs.

As seen in Figure 3a, the dye-coated particles outperform both the ligand-stripped and the as-synthesized samples at every size. Figure 3b quantifies the effect of dye sensitization by showing the UC quantum yield enhancement induced by dye adsorption (averaged across the irradiances studied) for each particle size. Considering the 10.9-nm particles, dye sensitization is observed to yield a 10x quantum yield increase over the corresponding ligand-stripped sample. This enhancement diminishes as particle diameter is increased but remains as high as 2x for the largest particles studied. Thus, as expected, smaller particles experience a greater enhancement when decorated with the fluorescent dye; importantly, however, the addition of the dye significantly increases quantum yield across all particle sizes. When comparing the dye-coated UCNPs to the as-synthesized ones, the size-dependence of the induced quantum

yield enhancement is less clear. In light of the findings of Wang et al. regarding the size-dependence of solvent-induced quenching,[50] however, we hypothesize that the convolution of the two dependences (i.e., those of dye-sensitized emission and solvent-mediated quenching) ultimately yields the trend observed in Figure 3b. Regardless, as is the case with respect to the ligand-stripped particles, it is clear that the dye-coated particles substantially outperform the as-synthesized samples despite being dispersed in a less favorable solvent.

Further insight can be gleaned from distinguishing between emission from the dye molecules and from Er^{3+} ions. This calculation is performed by first fitting the emission spectra used for quantum yield measurements to linear combinations of the dye emission spectrum and the Er^{3+} emission spectrum (see SI for details). After separating the total emission spectrum into constituent spectra in this fashion, the respective integrated emission intensities and therefore the quantum yield contributions of Er^{3+} and the dye can be calculated. Figure 3c depicts the fractions of the total quantum yield which arise from dye emission and from radiation from the Er^{3+} $^4F_{9/2}$ state. As the size of the nanoparticles is increased from 10.9 to 25.1 nm, the quantum yield contribution of the dye decreases from 90% to 73%; the balance is made up by Er^{3+} emission from the $^4F_{9/2}$ state (the $^2H_{11/2}$ and $^4S_{3/2}$ states in Er^{3+} contribute negligibly). This observation is consistent with the previous discussion regarding the size-dependence of dye effects; both the quantum yield fractions shown in Figure 3c as well as the dye-induced UC quantum yield enhancements highlighted in Figure 3b point to the hypothesized inverse relationship between nanoparticle size and dye impact.

Finally, we investigate excited-state lifetimes for the particles with and without dye to evaluate the importance of radiative rates. Figure 3d shows the lifetime of the Er^{3+} $^4S_{3/2} \rightarrow {}^4I_{15/2}$ transition as a function of size in all three sample sets. For all sample types, the lifetime is observed to increase with particle diameter. Moreover, the as-synthesized UCNPs exhibit longer lifetimes than do the ligand-stripped ones throughout the size regime studied. Because similar

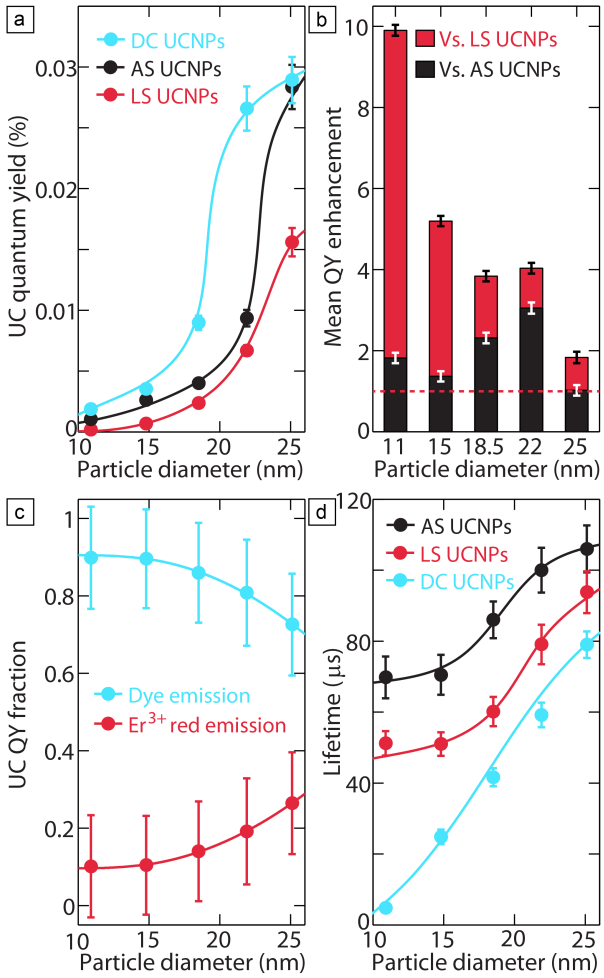

Figure 3: **Impact of emission sensitization on UC performance** a) UC quantum yield for all particle sizes and sample types; all values were obtained under 50 W/cm^2 of 980-nm illumination. Measurements were performed in solution with the dye-coated and ligand-stripped UCNPs dispersed in IPA and the as-synthesized particles suspended in cyclohexane. The dye-coated particles (cyan) are observed to significantly outperform both the as-synthesized (black) and the ligand-stripped particles (red) at all particle sizes, highlighting the promise of emission sensitization. b) UC quantum yield enhancement factor averaged across a series of irradiances ranging from 18 to 50 W/cm^2. A clear size dependence is visible with respect to the ligand-stripped UCNPs (red), yet even the 25-nm particles exhibit a 2x performance boost. The trend is less obvious in relation to the as-synthesized particles (black), likely the result of a convolution of size-dependent effects. c) Constituent fractions of the overall quantum yield corresponding to dye emission (cyan) and the Er^{3+} $^4F_{9/2}\rightarrow{}^4I_{15/2}$ transition (red). The contribution of the dye is observed to diminish with increasing particle size as expected. d) Decay lifetimes (here defined as the time necessary for emission intensity to reach half the initial value) for the Er^{3+} $^4S_{3/2}\rightarrow{}^4I_{15/2}$ transition for all sizes and sample sets. The dye-coated particles (cyan) exhibit much shorter lifetimes than do the ligand-stripped (red) and as-synthesized UCNPs (black), demonstrating dye-induced radiative rate enhancements.

trends are seen in UC quantum yield (i.e., UC quantum yield scales with size and is higher for as-synthesized particles than for ligand-stripped UCNPs), we infer that the corresponding lifetime increases arise from reductions to the nonradiative decay rate; this conclusion is consistent with the knowledge that larger particles and UCNPs dispersed in cyclohexane instead of in IPA are less prone to surface quenching. Conversely, that the dye-coated UCNPs exhibit the shortest lifetime yet also the highest quantum yield at all particle sizes is indicative of a greatly increased radiative rate. This lifetime reduction is unsurprising given the aforementioned 3.7-ns fluorescence lifetime reported by ATTO-TEC. We therefore conclude that the key characteristic responsible for the substantial quantum yield enhancements reported herein is the much faster radiative rate afforded by the dye molecules compared to Er^{3+}.

Briefly, we can rationalize the observed dependences of UC quantum yield enhancement and lifetime reduction on particle size by considering the energy transfer mechanics of the dye-coated UCNPs. Based on the high degree of spectral overlap between Er^{3+} green emission and the dye's absorption, we assume that the dominant energy transfer mechanism is Förster resonance energy transfer (FRET), as is the case for Yb-Er transfer events. FRET processes are extremely sensitive to the separation distance between the involved donor and acceptor species. Notably, because the dye molecules decorate the surfaces of the particles, only Er^{3+} ions which are sufficiently close to the surface will be able to directly transfer energy to the dye. And because the fraction of Er^{3+} ions inside this radius will vary with UCNP size in the same way as does the surface area-to-volume ratio, we anticipate the impact of the dye to be size-dependent. We can quantify this dependence by computing the FRET probability as a function of separation for dye-to-Er^{3+} transfer processes; doing so, we find a FRET efficiency of 0.98 for the smallest particles and one of 0.24 for the largest particles studied (see the SI for a detailed discussion of these calculations). The prevalence of rapid energy migration throughout the UCNP via Yb-Yb transfer events may somewhat mitigate this trend, but, as shown in Figure

3, a clear size dependence is experimentally evident. Recent publications by Muhr et al.[54] and by Dukhno et al.[55] provide rigorous and quantitative analyses of the energy transfer processes at play in similar UCNP-dye systems.

In addition to probing the size dependence of emission dye-sensitization, we explored the effect of dye surface coverage. Here, we decorate 18.5-nm particles with dye at target densities of one molecule per 112, 56, 28, 14, and 7 nm^2 of surface; these values correspond (assuming complete dye adsorption at all particle sizes) to dye:UCNP mass ratios of 0.0011, 0.0022, 0.0045, 0.009, and 0.018, respectively. Figure 4 summarizes the influence of dye density on UC performance enhancement. Shown in the inset, the UC quantum yield increase engendered by dye adsorption is independent of concentration over the range of 0.0011 to 0.009 in mass ratio. It is not until the highest density studied that the enhancement is affected in a discernible fashion: going from a ratio of 0.009 to 0.018, the observed quantum yield enhancement with respect to the ligand-stripped sample falls from 4x to 2.5x. In a similar study focusing on dye sensitization of UC absorption, Zou et al. observed an enhancement decrease at a similar dye:UCNP mass ratio. The researchers ascribed this decrease to a greater prevalence of deleterious dye-dye interactions (i.e., cross-relaxation) on the nanoparticle surfaces as well as to undesired absorption by unbound dye in solution.[47] While we do not anticipate the latter being an issue here (both because ATTO 542 has no absorption at 980 nm and because we centrifuge our samples to remove unbound dye), it is possible that cross-relaxation is occurring in our system.

Figure 4 also depicts how the excited-state lifetimes of the Er^{3+} $^4S_{3/2}\rightarrow{}^4I_{15/2}$ and $^4F_{9/2}\rightarrow{}^4I_{15/2}$ transitions as well as the dye emission vary with decoration density. In contrast to the quantum yield data, the lifetimes very clearly vary with surface density, and all three transitions are observed to occur more rapidly as the dye:UCNP mass ratio is increased. As discussed previously, while we do not expect the dye to siphon energy from the Er^{3+} $^4F_{9/2}$ manifold directly, the observed reduction in the $^4F_{9/2}\rightarrow{}^4I_{15/2}$ lifetime is unsurprising given the known role of the Er^{3+}

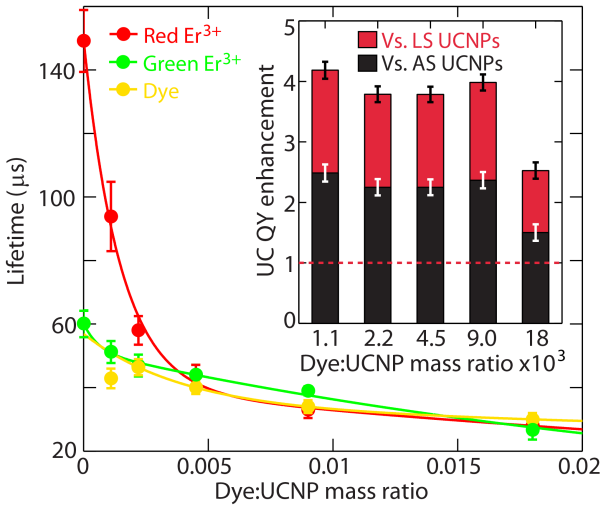

Figure 4: **Effect of dye surface density** Plot demonstrating the dependences of the Er^{3+} $^4F_{9/2} \rightarrow {}^4I_{15/2}$, Er^{3+} $^4S_{3/2} \rightarrow {}^4I_{15/2}$, and dye transition lifetimes (measured under 980-nm excitation) on dye surface density. The lifetime is again defined as the time required for the emission intensity to fall to half its initial value. As shown, the lifetime of each transition decreases as the dye:UCNP mass ratio is increased, suggesting that the radiative rates of the dye-coated UCNPs scale with dye coverage. The inset shows how the observed UC quantum yield increase with respect to the ligand-stripped particles (red) and to the as-synthesized particles (black) varies with coverage. Both factors remain constant until the highest density is reached, at which point a significant decrease is apparent. The dotted red line corresponds to unity.

$^2H_{11/2}$ and $^4S_{3/2}$ states as intermediates in the $^4F_{9/2}$ population mechanism.[45,46] Taken together, the lifetime and quantum yield enhancement data presented in Figure 4 provide mechanistic insight into the manner in which energy migrates within the dye-sensitized UCNPs. To reconcile the observed trends, we hypothesize that, given the high fluorescence yield of the dye and the probability of energy migration within the UCNP,[27,56] the maximum dye enhancement attainable for a given particle size is achieved with very little dye. Beyond this dye concentration, increasing the coverage simply reduces the time necessary for energy to reach a dye molecule (i.e., dye excitation is the rate-limiting step). Therefore, increasing the dye:UCNP mass ratio does not enable more radiation, but it increases the overall radiative rate. Importantly, however, much like the prior size-dependence investigation, the addition of the dye improves UC

performance in all cases studied.

In summary, we have demonstrated size-dependent enhancements in UC quantum yield by sensitizing emission with a fluorescent dye. Commercially available ATTO 542 is adsorbed onto the surfaces of β-$NaY_{0.8-x,y}Gd_xLu_yF_4$:$Yb_{0.18}Er_{0.02}$ UCNPs and successful decoration is confirmed via FTIR. The emission spectrum of the dye-coated nanoparticles under 980-nm illumination is observed to match that of the bare dye when excited directly, evincing successful energy transfer and subsequent dye emission. We find that dye sensitization significantly improves UC quantum yield across all particle sizes and incident powers, with the largest enhancement of 10x occurring for the 10.9-nm particles (the smallest studied). These quantum yield enhancements are coincident with excited-state lifetime reductions, confirming the cause of the dye-induced improvements to be the very fast radiative rate of the dye. Finally, further insight regarding the energy transfer sequences in the dye-coated UCNPs is gained by investigating the influence of dye surface density.

Our results point to the viability and impact of enhancing radiative rates in lanthanide-based upconverters. Importantly, emitting ions near the surface of the particle (which are completely quenched in conventional UCNPs[21]) are best able to couple to the dye molecules. This approach could inspire entirely new classes of particle design, including, for example, core-shell particles in which a core heavily doped with Yb^{3+} is encased within a thin, Er^{3+}-doped layer. Moreover, as demonstrated in this work, our approach yields greater enhancements for smaller particles. In conjunction with the fact that the resulting dye-coated UCNPs are water-soluble and stable under NIR illumination, our enhancement method may find broad application in biological imaging applications.

Acknowledgement

The authors gratefully acknowledge the assistance of Tarun Narayan, Shing Shing Ho, David Barton III, Alice Lay, Katherine Sytwu, and Randy Mehlenbacher. TEM characterization and XRD measurements were performed at the Stanford Nano Shared Facilities (SNSF). M.D.W. and J.A.D acknowledge financial support provided as part of the DOE "Light-Material Interactions in Energy Conversion" Energy Frontier Research Center under grant DE-SC0001293. S.F. and A.P.A. acknowledge support by the "Light-Material Interactions in Energy Conversion" Energy Frontier Research Center funded by the U.S. Department of Energy, Office of Science, Office of Basic Energy Sciences, under Contract DE-AC02-05CH11231, part of the EFRC at Caltech under DE-SC0001293. S.F. also acknowledges scholarship support from the German Research Foundation (DFG, agreement FI 2042/1-1). Additional funding was provided by the Global Climate and Energy Project at Stanford University.

Supporting Information Available

Additional details and further discussion regarding the experiments performed and the conclusions reached in this work.

This material is available free of charge via the Internet at `http://pubs.acs.org/`.

References

(1) Atre, A. C.; Dionne, J. A. Realistic upconverter-enhanced solar cells with non-ideal absorption and recombination efficiencies. *J. Appl. Phys.* **2011**, *110*, 034505.

(2) Boriskina, S. et al. Roadmap on optical energy conversion. *J. Opt.* **2016**, *18*, 073004.

(3) Briggs, J. A.; Atre, A. C.; Dionne, J. A. Narrow-bandwidth solar upconversion: Case studies of existing systems and generalized fundamental limits. *J. Appl. Phys.* **2013**, *113*, 124509.

(4) Fischer, S.; Favilla, E.; Tonelli, M.; Goldschmidt, J. C. Record efficient upconverter solar cell devices with optimized bifacial silicon solar cells and monocrystalline BaY_2F_8:30% Er^{3+} upconverter. *Sol. Energ. Mat. Sol. C.* **2015**, *136*, 127–134.

(5) Richards, B. S. Enhancing the performance of silicon solar cells via the application of passive luminescence conversion layers. *Sol. Energ. Mat. Sol. C.* **2006**, *90*, 2329–2337.

(6) Schulze, T. F.; Schmidt, T. W. Photochemical upconversion: present status and prospects for its application to solar energy conversion. *Energy Environ. Sci.* **2015**, *8*, 103.

(7) Shalav, A.; Richards, B. S.; Green, M. A. Luminescent layers for enhanced silicon solar cell performance: Up-conversion. *Sol. Energ. Mat. Sol. C.* **2007**, *91*, 829–842.

(8) Wang, H.-Q.; Batentschuk, M.; Osvet, A.; Pinna, L.; Brabec, C. J. Rare-earth ion doped up-conversion materials for photovoltaic applications. *Adv. Mater.* **2011**, *23*, 2675–2680.

(9) Strümpel, C.; McCann, M.; Beaucarne, G.; Arkhipov, V.; Slaoui, A.; Švrček, V.; del Cañizo, C.; Tobias, I. Modifying the solar spectrum to enhance silicon solar cell efficiency - An overview of available materials. *Sol. Energ. Mat. Sol. C.* **2007**, *91*, 238–249.

(10) Wang, H.-Q.; Stubhan, T.; Osvet, A.; Litzov, I.; Brabec, C. J. Up-conversion semiconducting MoO_3:Yb/Er nanocomposites as buffer layer in organic solar cells. *Sol. Energ. Mat. Sol. C.* **2012**, *105*, 196–201.

(11) Fischer, S.; Johnson, N. J. J.; Pichaandi, J.; Goldschmidt, J. C.; van Veggel, F. C. J. M. Upconverting core-shell nanocrystals with high quantum yield under low irradiance: On the role of isotropic and thick shells. *J. Appl. Phys.* **2015**, *118*, 193105.

(12) Goldschmidt, J. C.; Fischer, S. Upconversion for photovoltaics - a review of materials, devices, and concepts for performance enhancement. *Adv. Optical Mater.* **2015**, *3*, 510–535.

(13) Zhang, J.; Huang, Y.; Jin, L.; Rosei, F.; Vetrone, F.; Claverie, J. P. Efficient upconverting multiferroic core@shell photocatalysts: visible-to-near-infrared photon harvesting. *ACS Appl. Mater. Interfaces* **2017**, *9*, 8142–8150.

(14) Zhang, F.; Zhang, C.-L.; Peng, H.-Y.; Cong, H.-P.; Qian, H.-S. Near-infrared photocatalytic upconversion nanoparticles/TiO_2 nanofibers assembled in large scale by electrospinning. *Part. Part. Syst. Charact.* **2016**, *33*, 248–253.

(15) Tian, Q.; Yao, W.; Wu, W.; Liu, J.; Wu, Z.; Liu, L.; Dai, Z.; Jiang, C. Efficient UV-Vis-NIR responsive upconversion and plasmonic-enhanced photocatalyst based on lanthanide-doped $NaYF_4$/SnO_2/Ag. *ACS Sustainable Chem. Eng.* **2017**, *5*, 10889–10899.

(16) Zhou, B.; Shi, B.; Jin, D.; Liu, X. Controlling upconversion nanocrystals for emerging applications. *Nat. Nanotechnol.* **2015**, *10*, 924–936.

(17) Lu, Y. et al. Tunable lifetime multiplexing using luminescent nanocrystals. *Nat. Photonics* **2013**, *8*, 32–36.

(18) Deng, R.; Qin, F.; Chen, R.; Huang, W.; Hong, M.; Liu, X. Temporal full-colour tuning through non-steady-state upconversion. *Nat. Nanotechnol.* **2015**, *10*, 237–242.

(19) Liu, C.; Gao, Z.; Zeng, J.; Hou, Y.; Fang, F.; Li, Y.; Qiao, R.; Shen, L.; Lei, H.; Yang, W.; Gao, M. Magnetic/upconversion fluorescent $NaGdF_4$:Yb,Er nanoparticle-based dual-modal molecular probes for imaging tiny tumors in vivo. *ACS Nano* **2013**, *7*, 7227–7240.

(20) Carpenter, C. M.; Sun, C.; Pratx, G.; Liu, H.; Cheng, Z.; Xing, L. Radioluminescent nanophosphors enable multiplexed small-animal imaging. *Opt. Express* **2012**, *20*, 11598–11604.

(21) Gargas, D. J.; Chan, E. M.; Ostrowski, A. D.; Aloni, S.; Altoe, M. V. P.; Barnard, E. S.; Sanii, B.; Urban, J. J.; Milliron, D. J.; Cohen, B. E.; Schuck, P. J. Engineering bright sub-10-nm upconverting nanocrystals for single-molecule imaging. *Nat. Nanotechnol.* **2014**, *9*, 300–305.

(22) Zhou, J.; Liu, Z.; Li, F. Upconversion nanophosphors for small-animal imaging. *Chem. Soc. Rev.* **2011**, *41*, 1323–1349.

(23) Xiong, L.; Chen, Z.; Tian, Q.; Cao, T.; Xu, C.; Li, F. High contrast upconversion luminescence target imaging in vivo using peptide-labeled nanophosphors. *Anal. Chem.* **2009**, *81*, 8687–8694.

(24) Liu, Q.; Sun, Y.; Yang, T.; Feng, W.; Li, C.; Li, F. Sub-10 nm hexagonal lanthanide-doped $NaLuF_4$ upconversion nanocrystals for sensitive bioimaging in vivo. *J. Am. Chem. Soc.* **2011**, *133*, 17122–17125.

(25) Liu, Q.; Yang, T.; Feng, W.; Li, F. Blue-emissive upconversion nanoparticles for low-power-excited bioimaging in vivo. *J. Am. Chem. Soc.* **2012**, *134*, 5390–5397.

(26) Chatterjee, D. K.; Rufaihah, A. J.; Zhang, Y. Upconversion fluorescence imaging of cells and small animals using lanthanide doped nanocrystals. *Biomaterials* **2008**, *29*, 937–943.

(27) Li, J.; Zhu, X.; Xue, M.; Feng, W.; Ma, R.; Li, F. Nd^{3+}-sensitized upconversion nanostructure as a dual-channel emitting optical probe for near infrared-to-near infrared fingerprint imaging. *Inorg. Chem.* **2016**, *55*, 10278–10283.

(28) Naczynski, D. J.; Tan, M. C.; Zevon, M.; Wall, B.; Kohl, J.; Kulesa, A.; Chen, S.; Roth, C. M.; Riman, R. E.; Moghe, P. V. Rare-earth-doped biological composites as in vivo shortwave infrared reporters. *Nat. Commun.* **2013**, *4*, 2199.

(29) Chen, G.; Qiu, H.; Prasad, P. N.; Chen, X. Upconversion nanoparticles: design, nanochemistry, and applications in theranostics. *Chem. Rev.* **2014**, *114*, 5161–5214.

(30) Idris, N. M.; Gnanasammandhan, M. K.; Zhang, J.; Ho, P. C.; Mahendran, R.; Zhang, Y. In vivo photodynamic therapy using upconversion nanoparticles as remote-controlled nanotransducers. *Nat. Med.* **2012**, *18*, 1580–1585.

(31) Ai, X. et al. In vivo covalent cross-linking of photon-converted rare-earth nanostructures for tumour localization and theranostics. *Nat. Commun.* **2016**, *7*, 10432.

(32) Fischer, S.; Bronstein, N. D.; Swabeck, J. K.; Chan, E. M.; Alivisatos, A. P. Precise tuning of surface quenching for luminescence enhancement in core-shell lanthanide-doped nanocrystals. *Nano Lett.* **2016**, *16*, 7241–7247.

(33) Johnson, N. J. J.; He, S.; Diao, S.; Chan, E. M.; Dai, H.; Almutairi, A. Direct evidence for coupled surface and concentration quenching dynamics in lanthanide-doped nanocrystals. *J. Am. Chem. Soc.* **2017**, *139*, 3275–3282.

(34) Dodson, C. M.; Zia, R. Magnetic dipole and electric quadrupole transitions in the trivalent lanthanide series: Calculated emission rates and oscillator strengths. *Phys. Rev. B* **2012**, *86*, 125102.

(35) Wu, D. M.; García-Etxarri, A.; Salleo, A.; Dionne, J. A. Plasmon-enhanced upconversion. *J. Phys. Chem. Lett.* **2014**, *5*, 4020–4031.

(36) Renero-Lecuna, C.; Martín-Rodríguez, R.; Valiente, R.; González, J.; Rodríguez, F.; Krämer, K. W.; Güdel, H. U. Origin of the high upconversion green luminescence efficiency in β-$NaYF_4$:2%Er^{3+},20%Yb^{3+}. *Chem. Mater.* **2011**, *23*, 3442–3448.

(37) Wang, F.; Liu, X. Recent advances in the chemistry of lanthanide-doped upconversion nanocrystals. *Chem. Soc. Rev.* **2009**, *38*, 976–989.

(38) Wisser, M. D.; Chea, M.; Lin, Y.; Wu, D. M.; Mao, W. L.; Salleo, A.; Dionne, J. A. Strain-induced modification of optical selection rules in lanthanide-based upconverting nanoparticles. *Nano Lett.* **2015**, *15*, 1891–1897.

(39) Chan, E. M.; Gargas, D. J.; Schuck, P. J.; Milliron, D. J. Concentrating and recycling energy in lanthanide codopants for efficient and spectrally pure emission: The case of $NaYF_4$:Er^{3+}/Tm^{3+} upconverting nanocrystals. *J. Phys. Chem. B* **2012**, *116*, 10561–10570.

(40) Saboktakin, M.; Ye, X.; Chettiar, U. K.; Engheta, N.; Murray, C. B.; Kagan, C. R. Plasmonic enhancement of nanophosphor upconversion luminescence in Au nanohole arrays. *ACS Nano* **2013**, *7*, 7186–7192.

(41) Wisser, M. D.; Fischer, S.; Maurer, P. C.; Bronstein, N. D.; Chu, S.; Alivisatos, A. P.; Salleo, A.; Dionne, J. A. Enhancing quantum yield via local symmetry distortion in lanthanide-based upconverting nanoparticles. *ACS Photonics* **2016**, *3*, 1523–1530.

(42) Laporte, O.; Meggers, W. F. Some rules of spectral structure. *J. Opt. Soc. Am.* **1925**, *11*, 459–463.

(43) Wang, F.; Deng, R.; Liu, X. Preparation of core-shell $NaGdF_4$ nanoparticles doped with luminescent lanthanide ions to be used as upconversion-based probes. *Nat. Protoc.* **2014**, *9*.

(44) Cattley, C. A.; Stavrinadis, A.; Beal, R.; Moghal, J.; Cook, A. G.; Grant, P. S.; Smith, J. M.; Assender, H.; Watt, A. A. R. Colloidal synthesis of lead oxide nanocrystals for photovoltaics. *Chem. Commun.* **2010**, *46*, 2802–2804.

(45) Anderson, R. B.; Smith, S. J.; May, P. S.; Berry, M. T. Revisiting the NIR-to-visible upconversion mechanism in β-$NaYF_4$:Yb^{3+},Er^{3+}. *J. Phys. Chem. Lett.* **2014**, *5*, 36–42.

(46) Berry, M. T.; May, P. S. Disputed mechanism for NIR-to-red upconversion luminescence in $NaYF_4$:Yb^{3+},Er^{3+}. *J. Phys. Chem. A* **2015**, *119*, 9805–9811.

(47) Zou, W.; Visser, C.; Maduro, J. A.; Pshenichnikov, M. S.; Hummelen, J. C. Broadband dye-sensitized upconversion of near-infrared light. *Nat. Photonics* **2012**, *6*, 560–564.

(48) Wu, X.; Zhang, Y.; Takle, K.; Bilsel, O.; Li, Z.; Lee, H.; Zhang, Z.; Li, D.; Fan, W.; Duan, C.; Chan, E. M.; Lois, C.; Xiang, Y.; Han, G. Dye-sensitized core/active shell upconversion nanoparticles for optogenetics and bioimaging applications. *ACS Nano* **2016**, *10*, 1060–1066.

(49) Zhang, Y.; Huang, L.; Li, Z.; Ma, G.; Zhou, Y.; Han, G. Illuminating cell signaling with near-infrared light-responsive nanomaterials. *ACS Nano* **2016**, *10*, 3881–3885.

(50) Wang, F.; Wang, J.; Liu, X. Direct evidence of a surface quenching effect on size-

dependent luminescence of upconversion nanoparticles. *Angew. Chem.* **2010**, *122*, 7618–7622.

(51) Boyer, J.-C.; Manseau, M.-P.; Murray, J. I.; van Veggel, F. C. J. M. Surface modification of upconverting $NaYF_4$ nanoparticles with PEG-phosphate ligands for NIR (800 nm) biolabeling within the biological window. *Langmuir* **2010**, *26*, 1157–1164.

(52) Boyer, J.-C.; van Veggel, F. C. J. M. Absolute quantum yield measurements of colloidal $NaYF_4$: Er^{3+}, Yb^{3+} upconverting nanoparticles. *Nanoscale* **2010**, *2*, 1417–1419.

(53) Yuan, D.; Tan, M. C.; Riman, R. E.; Chow, G. M. Comprehensive study on the size effects of the optical properties of $NaYF_4$:Yb,Er nanocrystals. *J. Phys. Chem. C* **2013**, *117*, 13297–13304.

(54) Muhr, V.; Würth, C.; Kraft, M.; Buchner, M.; Baeumner, A. J.; Resch-Genger, U.; Hirsch, T. Particle-size-dependent Förster resonance energy transfer from upconversion nanoparticles to organic dyes. *Anal. Chem.* **2017**, *89*, 4868–4874.

(55) Dukhno, O.; Pryzbilla, F.; Collot, M.; Klymchenko, A.; Pivovarenko, V.; Buchner, M.; Muhr, V.; Hirsch, T.; Mély, Y. Quantitative assessment of energy transfer in upconverting nanoparticles grafted with organic dyes. *Nanoscale* **2017**, *9*, 11994–12004.

(56) Prorok, K.; Pawlyta, M.; Strek, W.; Bednarkiewicz, A. Energy migration up-conversion of Tb^{3+} in Yb^{3+} and Nd^{3+} codoped active-core/active-shell colloidal nanoparticles. *Chem. Mater.* **2016**, *28*, 2295–2300.

Graphical TOC Entry